Journal of Materials Chemistry A

ROYAL SOCIETY OF CHEMISTRY

PAPER

View Article Online
View Journal | View Issue

Check for updates

Cite this: J. Mater. Chem. A, 2023, 11, 16714

Synergizing plasmonic Au nanocages with 2D MoS_2 nanosheets for significant enhancement in photocatalytic hydrogen evolution†‡

Rui Peng,§[a] Xiaohan Ma, §[ab] Zachary D. Hood,[c] Abdelaziz Boulesbaa, [d] Alexander A. Puretzky,[a] Jianhua Tong [b] and Zili Wu *[a]

Plasmonic enhancement of photocatalytic hydrogen evolution has been achieved under visible light illumination by integrating strongly plasmonic metal particles such as gold (Au) with semiconducting materials. To understand the effect of plasmon resonance on the photocatalytic hydrogen evolution reaction (HER), in this work, we study the hydrogen evolution reaction (HER) over Au nanocages with systematically tunable localized surface plasmon resonance (LSPR) properties dispersed on an Al_2O_3 support and covered with multiphasic 2D MoS_2 nanosheets. It is interesting to observe that by tuning the LSPR wavelength of Au nanocages, an optimal enhancement in the photocatalytic HER can be obtained over the multiphasic 2D MoS_2 nanosheets. In particular, when the LSPR wavelength of Au nanocages is close to the absorption edge of MoS_2 nanosheets, a 40-fold increase is observed in the HER rate regarding bare MoS_2. Time-resolved transient absorption spectroscopy was conducted to explicitly identify the mechanisms behind the Au/MoS_2 system. The results suggest that near field enhancement (NFE) is the dominant LSPR process in this system and a detailed explanation of the working mechanism in this system is proposed. Governed by the NFE process, the energy of the surface plasma is transferred from Au nanocages to MoS_2 nanosheets to promote electron–hole excitation in MoS_2, and the efficiency reaches the maximum when the LSPR wavelength of Au nanocages matches the MoS_2 light absorption edge, resulting in a significantly enhanced photocatalytic hydrogen yield compared to the bare MoS_2 nanosheets and Au/MoS_2 systems where the LSPR wavelengths of Au nanocages and MoS_2 nanosheet absorption edge do not match. The learning from this work provides insights into the design of highly efficient photocatalysts based on plasmonic materials.

Received 20th March 2023
Accepted 11th July 2023

DOI: 10.1039/d3ta01657a

rsc.li/materials-a

Introduction

Earth-abundant transition metal dichalcogenides (TMDs) represent a class of emerging materials for solar energy conversion.[1–5] Among these TMDs, MoS_2 has received the most intense interest owing to its balanced hydrogen bonding Gibbs free energy on its edge site.[6,7] In our recent work,[8] we have successfully activated the basal plane in a single-layer MoS_2 nanosheet consisting of both 2H (semiconducting) and 1T-like (metallic) phases for photocatalytic hydrogen evolution from water splitting. These multiphasic MoS_2 nanosheets possess properties that are favorable for light absorption and hydrogen evolution,[9–13] yet their photocatalytic performance is to be further improved.

Recently, plasmonic metals have been widely studied as effective materials to boost the overall activity of semiconductor-based photocatalysis, especially for solar hydrogen production.[14–18] Photoinduced localized surface plasmon resonance (LSPR) can be activated in plasmonic metal species with irradiation using suitable light sources. The working mechanisms of LSPR-enhanced photocatalysis are

[a]Center for Nanophase Materials Sciences, Oak Ridge National Laboratory, Oak Ridge, Tennessee 37831, USA. E-mail: wuz1@ornl.gov

[b]Department of Materials Science and Engineering, Clemson University, Clemson, South Carolina 29634, USA

[c]Applied Materials Division, Argonne National Laboratory, 9700 S. Cass Avenue, Lemont, Illinois 60439, USA

[d]Department of Chemistry and Biochemistry, California State University Northridge, Northridge, California 91330, USA

‡ Electronic supplementary information (ESI) available. See DOI: https://doi.org/10.1039/d3ta01657a

§ These authors contributed equally to this work.

quite complicated due to several possible concurrent ones including hot-electron transfer (HET), near-field enhancement (NFE) and plasmon resonant energy transfer (PRET).[17–21] Besides, as metal materials, plasmonic metal species can also accept photogenerated electrons from a semiconductor through a classic electron transfer pathway, which makes the process even more complex.

For HET, disequilibrium arrangement of the electrons in the metal nanostructure and surface "hot electrons" can be generated by LSPR. As the metal species are coupled with a semiconductor, LSPR-induced hot electrons can be injected into the conduction band of the semiconductor that is in contact with the metal, which is a nonradiative process.[17–21]

NFE, however, is a radiative process. The near electromagnetic field generated by the plasmon dipole on a metal surface can significantly enhance the inter-band or other optical transitions in the nearby semiconductor (not necessarily in contact) as the generated field is typically orders of magnitude higher than the incident light.[20–22] Therefore, the plasmonic metal is acting like a secondary light source and transferring the energy to the semiconductor. One feature of the radiative process is that the emitted photon will possess the same energy as the absorbed photon.[22] Therefore, NFE requires a match of LSPR wavelength to the absorption edge of the semiconductor to maximize the process efficiency.

For PRET, the energy can be transferred from plasmonic metal species to semiconductors to generate excited electrons through nonradiative dipole–dipole coupling between the plasmonic dipole and electron–hole exciton in semiconductors.[20,21] Like NFE, no direct contact between the metal and semiconductor is required for PRET, but the energy transfer efficiency highly depends on the spectrum overlap between the plasmonic metal and semiconductor and the special distance between the two parts.[18,20–22] Additionally, it has a reverse and competing process called Förster resonant energy transfer (FRET), where energy will transfer from the semiconductor to the plasmonic metal. It becomes stronger when the spatial separation between the metal and semiconductor becomes larger.[23]

Although the explicit mechanism of charge transport between a plasmonic metal and semiconductor remains controversial, with the strong contribution from plasmonic metal nanostructures, photocatalytic efficiency over the semiconductor species can be drastically enhanced, indicating the positive influence of the plasmonic metals in the photocatalysis process.[19,24,25]

As a famous plasmonic metal, various plasmonic Au nanostructures, such as Au nanorods,[26–29] nanoplates,[29,30] nanocubes,[29,31,32] nanoantennae,[30,33] and nanoparticles[16,34–36] have been reported to couple with MoS_2 nanosheets to investigate the plasmonic effect on the electronic and/or optical behaviors of MoS_2. While the shape effect of plasmonic metal nanostructures on LSPR behaviors has become a hot topic, the LSPR wavelength, another pivotal parameter of plasmonic metal nanostructures, has received much less attention. So far, only limited work has been conducted to reveal how the variation of their various LSPR absorption behaviors impacts the activity of the photocatalyst system.[37–40] For example, it has been proposed that PRET may compete with HET when LSPR wavelength is close to the adsorption edge of the semiconductor in an Ag@Cu_2O core–shell system and hence suppress the plasmonic enhancement.[39] Yue *et al.*[40] reported a Au–Ag/CdS catalyst system, which was composed of CdS as the semiconductor and Au–Ag nanoparticles (NPs) as the plasmonic nanostructure. The Au–Ag NPs were prepared by galvanic replacement. By adjusting the synthesis parameters, the LSPR wavelength of Au–Ag NPs can be finely tuned to a desired frequency. With the help of this feature, they found that excess absorption spectral overlap between the plasmonic metal and semiconductor can lead to a decrease in activity.[40] However, a comprehensive understanding of the system was still lacking as they only considered the PRET process of LSPR.

To further understand the plasma-induced photocatalytic enhancement effect, we intentionally designed a series of photocatalysts composed of 2D MoS_2 nanosheets loaded with Au nanocages. First reported by Xia's group in 2007,[41] Au nanocages are in nature Au shells on the surface of Ag nanocubes. They are similar to the Au–Ag NPs mentioned above as both of them are Au/Ag heterostructures prepared by galvanic replacement and their LSPR wavelength can be finely tuned. Differently, considering the shape effect, Au nanocages can impose a stronger LSPR effect than the sphere-like Au–Ag NPs as Au nanocages have sharper features.[22,42] The stronger LSPR effect around their edges and corners[22] can lead to a greater impact on photocatalytic performance, making it easier to be observed and analyzed.

In this paper, we aimed to synergize the merits of multiphasic 2D MoS_2 and Au nanocages with different LSPR wavelengths and investigate the impact of Au LSPR adsorption behavior on the photocatalytic performance of the system in a more comprehensive and profound way. In this study, the hydrogen evolution reaction (HER) was adopted as a model reaction. It was found that all the Au/MoS_2 systems showed better HER performance than bare MoS_2 after the loading of Au nanocages, but a particularly large rate enhancement of up to 40 fold (regarding bare MoS_2) was observed when the LSPR wavelength of the Au nanocages matched the absorption edge of MoS_2. The underlying mechanism was characterized with microscopy and optical and time-resolved transient absorption spectroscopy of the Au nanocages and MoS_2 nanosheets.

Experimental

Synthesis

Synthesis of chemically exfoliated MoS_2. The synthesis of exfoliated, multiphasic MoS_2 nanosheets followed our previous report.[8] Briefly, a bulk MoS_2 sample (ultrafine powder obtained from Graphene Supermarket) was dried in a vacuum oven at room temperature for 2 days to remove the adsorbed water molecules on the surface. Afterward, the dried MoS_2 sample was transferred to an argon-filled glovebox. Then bulk MoS_2 was added to a Li superhydride solution [1.0 M in tetrahydrofuran (THF), Sigma-Aldrich] with a concentration of 10 mg mL^{-1}. The mixed solution was sealed in an air-tight round bottom flask.

After this, the round-bottomed flask was discharged from the glove box and placed in a sonication bath at room temperature. The mixed solution was sonicated for 2 h to allow thorough diffusion of the Li sources into the layers of pristine MoS_2. Subsequently, the round-bottomed flask was placed into an oil bath and heated at 100 °C for 5 days. The sample was then washed with THF (≥99.0%, Sigma-Aldrich) four times at room temperature to remove excessive Li precursors and organic residues from the sample. Finally, the Li_xMoS_2 sample was dried under an argon atmosphere at room temperature. In order to obtain exfoliated ultrathin MoS_2 nanosheets, the freshly prepared Li_xMoS_2 sample was dispersed in de-ionized (D.I.) water (18.2 MΩ cm^{-1}). Upon the addition of Li_xMoS_2 to D.I. water, continuous bubbles can be observed, which is ascribed to the formation of hydrogen gas. The mixture was then subjected to an additional 1 h of sonication in an ice bath to maintain the temperature. After sonication, the mixed solution was centrifuged several times to remove the unexfoliated MoS_2 while simultaneously washing out excess Li residues from the sample. The exfoliated MoS_2 was collected and stored at room temperature for further use.

Synthesis of Ag nanocubes. Ag nanocubes with an edge length of 45–50 nm were prepared using a previously reported protocol.[43] In brief, 50 mL of ethylene glycol (EG) was preheated at 150 °C for 30 min. During this time, four separate solutions were prepared: (1) 2.0 mg NaSH in 11.89 mL EG (sample concentration: 3 mM), (2) 3 μL HCl in 12 mL EG (sample concentration: 3 mM), (3) 0.3500 g polyvinylpyrrolidone (PVP) (MW ≈ 55 000) in 17.5 mL EG, and (4) 0.3000 g CF_3COOAg (>99.99% metal basis, Aldrich) dissolved in 4.18 mL EG (sample concentration 282 mM). Each of these solutions was sufficiently stirred to dissolve the precursors. Next, 0.6 mL of (1) was added to the EG solution at 150 °C. After 4 minutes, 5 mL of (2) was added to the reaction. After another 2 minutes, 12.5 mL of (3) was added to the reaction. After another 2 minutes, 4 mL of (4) was added to the reaction. The reaction was cooled in an ice bath after ~60 min. The Ag nanocubes were purified by dispersing the products of the reaction in acetone and collecting them by centrifugation at 4900 rpm for 8 min. The Ag nanocubes were washed three times in D.I. H_2O (18.2 MΩ cm^{-1}), collected by centrifugation at 14 000 rpm for 15 min, and combined in 8 mL of D.I. H_2O to create a stock solution of Ag nanocubes.

Synthesis of Au nanocages. Au nanocages were prepared by galvanic replacement with $HAuCl_4$.[44,45] Briefly, 1.000 mL of the stock solution of Ag nanocube solution was added to 20 mL of D.I. H_2O (18.2 MΩ cm^{-1}) and preheated for 20 min at 90 °C. A syringe (BD plastic, 30 mL) was filled with a freshly prepared stock solution of $HAuCl_4$ (0.75 mM, 20 mL), which was injected into the Ag nanocube solution at a rate of 4.5 mL h^{-1}. The reaction was monitored by UV-vis spectroscopy, and once the desired localized surface plasmon resonance was reached (460, 680, and 750 nm), the reaction was cooled in an ice water bath, stirred for 1 h with excess NaCl to form $AgCl_4^{3-}$, and centrifuged at 10 000 rpm for 20 min. The pellet containing Au nanocages was washed five times by re-dispersing in 25 mL D.I. H_2O and centrifuging at 10 500 rpm. The as prepared Au nanocages were labeled as Au-460, Au-680 and Au-750 based on their respective LSPR wavelengths.

Assembly of Au/MoS_2–Al_2O_3 photocatalysts. The photocatalysts for solar hydrogen production were assembled by depositing Au nanocages and exfoliated MoS_2 nanosheets onto Al_2O_3 (Sigma-Aldrich, surface area: 155 m^2 g^{-1}) support materials. 0.6 g of Al_2O_3 were added into 5 mL of synthesized aqueous Au nanocage solution and sonicated for 2 h to achieve the intended 0.5 wt% of Au. The sample was collected by centrifugation and dried at room temperature. Subsequently, the dried powder sample was dispersed into 10 mL as-prepared MoS_2 solution to obtain 0.33 wt% MoS_2. The mixed solution was shaken vigorously for 2 h. At last, the final product was collected again by centrifugation and dried at room temperature. For the sake of conciseness, the samples were labeled as AMA-460, AMA-680, and AMA-750 in which AMA stands for Au, MoS_2, and Al_2O_3 and the number indicates the LSPR wavelength of the Au nanocages.

Photocatalytic hydrogen evolution reaction. In a typical photocatalytic experiment, 40 mg of the photocatalyst was dispersed in a solution composed of 30 mL deionized water and 10 mL methanol (Alfa Aesar) as electron donors in a quartz reactor. Prior to the photocatalytic reaction, the quartz cell was purged by continuous flushing with ultrahigh pure argon gas for 30 min. The light input is provided by a 200 W Hg lamp equipped with a cut-off filter to allow the passage of visible light with wavelength longer than 400 nm. The suspension was stirred vigorously during the entire photocatalytic reaction and the temperature of the system was maintained at 25 °C using the cooling water circulating around the entire quartz cell. The yielded hydrogen gas was determined and quantified using gas chromatography (GC) compiled with a hydrogen calibration plot, with model BUCK 910 (molecular sieve column, TCD detector, and argon as carrier gas). The photocatalytic hydrogen production rate was calculated by normalizing the produced hydrogen to the amount of MoS_2 in the catalysts per hour.

Characterization

Powder X-ray diffraction (XRD) patterns of the AMA samples were recorded using a PANalytical X'Pert Pro powder diffractometer equipped with Ni-filtered Cu Kα radiation. Scanning electron microscopy (SEM) images of exfoliated MoS_2 nanosheets deposited on a Si wafer were collected with a Zeiss Merlin SEM at 3.0 kV. The transmission electron microscopy (TEM) images of exfoliated MoS_2 nanosheets deposited on a lacy carbon grid were recorded on an aberration-corrected FEI Titan S 80-300 TEM/scanning transmission electron microscopy (STEM) operated at 300 kV with a Gatan charge coupled device (CCD) camera. STEM-X-ray energy dispersive spectroscopy (STEM-EDS) was performed on an FEI Talos F200X equipped with an EDS detector (Bruker) operated at 200 kV. Elemental maps were collected with a STEM spot size of 6. Raman and photoluminescence spectra of the exfoliated MoS_2 aqueous sample were recorded on an Acton TriVista 555 spectrometer (Princeton Instruments) with laser excitation at 532 nm. Diffuse reflectance spectroscopy (DRS) analysis of the AMA samples was

carried out using a Cary 5000 UV-visible spectrophotometer equipped with a praying mantis diffuse reflectance accessory. X-ray photoelectron spectroscopy (XPS) measurements were performed on each powder sample (MoS_2–Al_2O_3) with a Thermo Scientific K-Alpha spectrometer. All spectra were collected using an Al Kα microfused monochromatized source (1486.6 eV) with a step size of 0.1 eV over 50 scans. For all spectra, the spot size was 400 μm and the operating pressure was under 3.0×10^{-7} mbar.

Femtosecond transient absorption measurements of the Au/MoS_2 deposited on a glass slide were carried out on a home-built pump-probe spectrometer (PPS). A full description of the PPS can be found elsewhere.[46] Briefly, the PPS is based on a titanium sapphire (Ti:Sa) oscillator (Micra, Coherent) with its output seeded using a Ti:Sa Coherent Legend amplifier (USP-HE) operating at a 1 kHz repetition rate. The amplifier provides pulses centered at 800 nm, with ~45 fs duration and 2.2 mJ energy per pulse. The output of the Legend amplifier was divided into two portions: 90% was attenuated to 0.5 mJ and focused on a BBO crystal to generate a 400 nm pump pulse. The second portion (10%) was used to generate a white light continuum (WLC) probe in a 2 mm thick sapphire window. The WLC, which covers the spectral range from 450 nm to 900 nm, was collimated after generation and focused onto the sample using high reflective parabolic mirrors to minimize temporal chirp. After this, the transmitted probe was focused onto a 100-micron core fiber coupled with a spectrometer linear CCD array (USB2000ES, Ocean Optics). The pump passes through a controllable stage-delay and was chopped at 500 Hz frequency to allow the measurement of absorbance change in the transmitted probe between each two successive laser shots. At the sample, the pump and probe spot sizes were 100 and 50 μm, and the pump energy was ~4 μJ cm^{-2}.

Results and discussion

Structure and morphology

In order to investigate the crystallographic structures of the AMA samples, powder XRD was employed. Fig. 1A shows the XRD patterns of the composite AMA samples along with a pure Al_2O_3 support material. The XRD patterns of the Au and MoS_2 incorporated samples exhibit a pattern similar to that of Al_2O_3, *i.e.*, intrinsic diffraction peaks of Al_2O_3 can be observed from all the samples. A few small diffraction peaks falling at 18.1° can be assigned to the presence of $Al_2O_3 \cdot 3H_2O$ (PDF: 00-001-0259). No peak of Au or MoS_2 can be observed due to their low loading on Al_2O_3.

Similar to our previous work,[8] Raman spectroscopy is applied to identify the 2D and multiphasic nature of the as-synthesized MoS_2 nanosheets. The Raman spectrum of the freshly prepared MoS_2 aqueous suspension is shown in Fig. 1B. The typical in-plane mode (E^1_{2g}) and out-of-plane mode (A_{1g}) peaks of the MoS_2 sample can be observed at 388 and 409 cm^{-1}. Compared with those (385 and 410 cm^{-1}) of bulk MoS_2, the shift of the two peaks indicates the effective exfoliation of the Li intercalated MoS_2 layers and the presence of single-layer MoS_2.[47] In addition to the E^1_{2g} and A_{1g} vibration modes, the

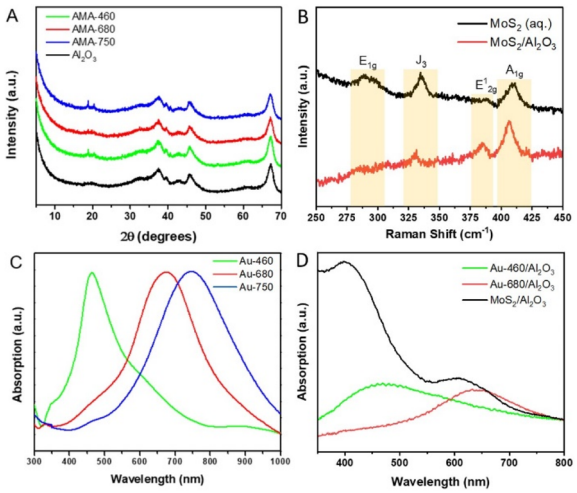

Fig. 1 (A) XRD patterns of Al_2O_3 supported Au/MoS_2 samples. (B) Raman spectra of the as-exfoliated MoS_2 nanosheets suspended in water (black) and loaded on Al_2O_3 (red). (C) UV-vis absorption spectra of the as-synthesized three Au nanocages. (D) UV-vis DRS of Au-460, Au-680 and MoS_2 nanosheets loaded on Al_2O_3.

exfoliated MoS_2 nanosheets also present two unique peaks at around 285 (E_{1g}) and 333 cm^{-1} (J_3), both of which originate from the metallic 1T-like phase of MoS_2 formed during the Li intercalation.[8,48] Specifically, the Raman spectrum of MoS_2/Al_2O_3 is also inspected to see if there is any structure change after the loading on Al_2O_3. Although the E_{1g} peak becomes less obvious, the existence of J_3 still reveals the existence of a 1T-like phase. Meanwhile, although there is a slight peak shift for E^1_{2g} (from 388 to 386 cm^{-1}) and A_{1g} (from 409 to 407 cm^{-1}), probably caused by the dielectric effect of Al_2O_3, the separation between these two peaks is almost unchanged after the loading process, suggesting that the MoS_2 nanosheets are well dispersed and do not restack on Al_2O_3.

The AFM image and the layer thickness profiles of the three representative nanosheets displayed in Fig. 2 demonstrate that the majority of the MoS_2 nanosheets are about 1 nm thick. This also confirms the successful preparation of single-layer MoS_2. Combining the SEM images of these exfoliated nanosheets (shown in Fig. S1 in the ESI‡) and from our previous work on the same MoS_2 system,[8] it can be concluded that monolayered multiphasic MoS_2 nanosheets have been successfully obtained by following our preparation procedures.

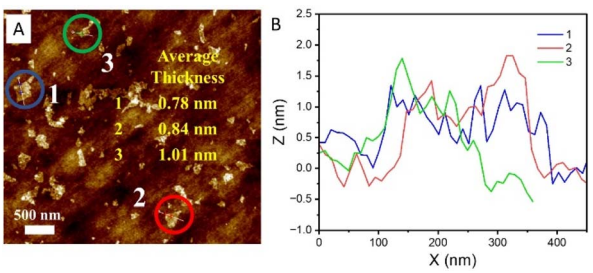

Fig. 2 (A) AFM image of the as-exfoliated single-layer and (B) the height profiles of three selected regions indicated in the figure.

The LSPR of the Au nanocages is verified before dispersing onto the Al_2O_3 support. The Au nanocages are prepared *via* galvanic replacement between Ag nanocubes and $HAuCl_4$ in an aqueous solution set to 90 °C, similar to our previous reports.[44] To systematically investigate the effect of the LSPR on the performance of photocatalytic activity over MoS_2 samples for the photocatalytic HER, the LSPR of the Au nanocages was tuned to three different wavelengths: 460, 680, and 750 nm (Fig. 1C) that are off, on, and off the light absorption edge of MoS_2. Fig. 1D displays the UV-vis diffuse reflectance spectra (DRS) of the Au nanocages loaded on Al_2O_3. Only a slight peak shift is observed that does not affect the positions relative to each other. A good match between the absorption edge of MoS_2 and the LSPR wavelength of Au-680 can also be observed from the spectra. The as-synthesized Au nanocages have an average size of 48 ± 3.5 nm as measured by transmission electron microscopy (TEM) (Fig. S2‡). When Au nanocages are titrated with different amounts of $HAuCl_4$, their wall thickness changes and pushes the LSPR towards the near-infrared spectral region.

To investigate the heterojunction between gold nanocages and MoS_2 nanosheets, we prepared a representative sample for high-angle annular dark-field (HAADF) scanning transmission electron microscopy (STEM) and bright-field STEM (BF-STEM) imaging. Fig. 3 shows the BF- and HAADF-STEM images of the AMA-680 sample as a representative. The BF-STEM images clearly reveal the lattice for the gold nanocage and a honeycomb structure for MoS_2. We also investigated the elemental distribution of Au, Mo, S, Ag and Al in the AMA-680 sample by energy-dispersive X-ray spectroscopy (EDS) based on STEM. The STEM-EDS elemental mappings are shown in Fig. S3,‡ where the Au nanocage is clearly seen in contact with MoS_2, as expected, on the Al_2O_3 support. However, it should be noticed that due to the tremendous morphology and size differences between the Au nanocages and MoS_2 nanosheets, some of the MoS_2 nanosheets are not in contact with Au, which can also be observed from Fig. S3.‡

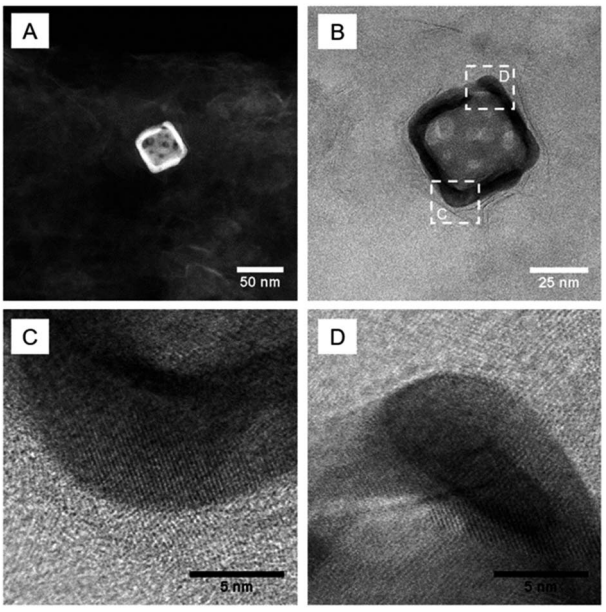

Fig. 3 Representative (A) HAADF- and (B–D) BF-STEM images of the AMA-680 sample.

The phase properties of the chemically exfoliated MoS_2 are evaluated by X-ray photoelectron spectroscopy (XPS). It must be noted that the thermodynamically stable form of MoS_2 is the 2H phase, where each Mo is prismatically coordinated with six S atoms. The 1T-like phase, on the other hand, is composed of octahedrally coordinated Mo with six S atoms. The structure of MoS_2 has been previously reported to undergo a structural transformation from the 1T-like into the 2H phase by thermal treatment between room temperature and 300 °C.[8] XPS is then employed to further investigate the multiphasic properties of 2D MoS_2 in different AMA samples (Fig. 4). The Mo 3d spectra (Fig. 4A) consist of peaks at around 229 and 232 eV, corresponding to Mo^{4+} $3d_{5/2}$ and Mo^{4+} $3d_{3/2}$, respectively. Deconvolution of the Mo 3d spectra reveals a shift in the spectra to higher binding energies (by ~0.9 eV) when the MoS_2 nanosheets are annealed at increased temperatures (*e.g.*, 60 and 120 °C). This shift to higher binding energies can be attributed to the phase transformation from the metallic 1T-like phase into the 2H phase (Table S1‡). The S 2p spectra shown in Fig. 4B display a similar shift to higher binding energies when multiphasic MoS_2 is annealed at increased temperatures. The S 2p spectra display doublet peaks, S $2p_{1/2}$ and S $2p_{3/2}$, appearing at ~163 and ~161.9 eV, respectively. Deconvolution of these peaks clearly illustrates the phase shift from the metallic 1T-like phase to the 2H phase when the samples are annealed at 60 and 120 °C. It is worth noting that no peaks are observed from 235 to 240 eV, suggesting that oxidation of Mo^{4+} to Mo^{6+} is minimal. The oxidation state and thermal stability of the Au nanocages are also investigated by XPS and TEM imaging after the thermal annealing at 60 and 120 °C. XPS measurements are also performed on the Au 4f region for the different gold nanocages. As shown in Fig. 4C, the Au 4f region shows clear doublet peaks at 84.0 and 87.7 eV, corresponding to Au^0 $4f_{5/2}$ and Au^0 $4f_{7/2}$, respectively. TEM images of the Au nanocages before and after heat treatment at 60 and 120 °C show that the gold nanocages retain their morphology (Fig. S4‡).

UV-vis DRS is conducted to investigate the optical properties of the Au/MoS_2–Al_2O_3 samples. Fig. S5A‡ displays the spectra of the AMA samples assembled with various Au nanocages. All the spectra in Fig. S5A‡ are similar to each other, a result of the strong light absorption by MoS_2. Several absorption bands in the visible light region can be observed in these samples. Two strong absorption peaks that belonged to typical MoS_2 are observed in all the samples. The one at ~420 nm corresponds to convoluted C and D excitonic and the one at ~620 nm corresponds to A and B excitonic peaks arising from the *K* point of the Brillouin zone.[9] Due to the high intensity of these two peaks, the absorption of Au-460 and Au-680 is eclipsed. However, Au-750 presents an appreciable and broad absorption band at ~750 nm that can be clearly monitored. We also performed UV-vis DRS on the annealed AMA-680 samples and their spectra are shown in Fig. S5B.‡ It can be seen that all the samples display similar absorption curves indicating the similar chemical composition of the samples after heat treatment.

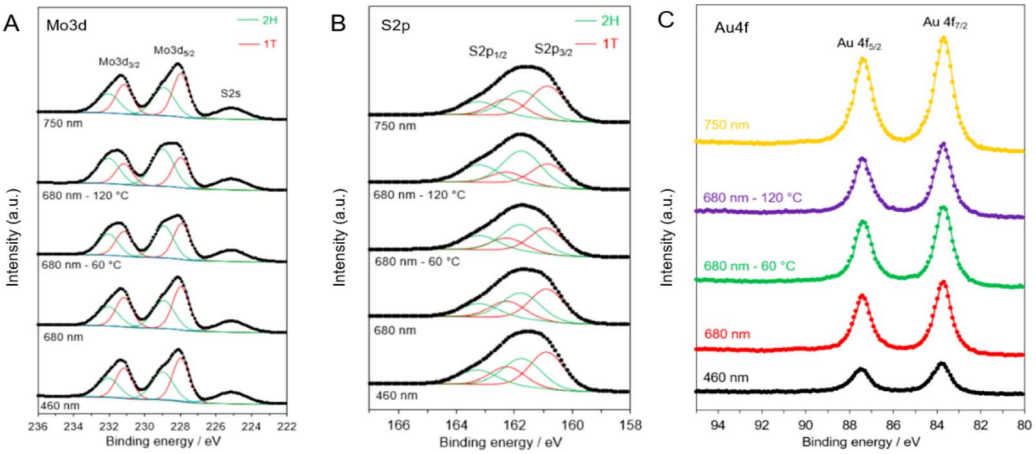

Fig. 4 XPS spectra of (A) Mo 3d, (B) S 2p, and (C) Au 4f core level regions of the various AMA samples.

Photocatalytic performance

In order to investigate the LSPR effect on the photocatalytic HER performance, the activity of the AMA samples is studied under identical experimental conditions. Fig. 5 shows the kinetic plot of the AMA samples in terms of the hydrogen evolution rate normalized to MoS_2 weight as a function of reaction time. It can be seen that compared with the pure MoS_2 sample, all Au-containing samples exhibit over an order of magnitude enhancement in the hydrogen evolution rate. This phenomenon is thought to be the result of the LSPR effect from Au nanocages. These surface plasmas arising from Au nanocages have been proven to be beneficial factors during the photocatalytic hydrogen evolution reaction.[49,50] Interestingly, it can be seen that the AMA-680 sample presents a strikingly higher photocatalytic hydrogen evolution rate compared with the other two AMA samples. As shown in Fig. 5A and C, a ~40-fold increase in the hydrogen evolution rate is obtained on AMA-680 over the bare MoS_2 nanosheets while about a 15-fold increase is found on the other two AMA samples. The superior photocatalytic activity of the AMA-680 sample may be rationalized by the more efficient energy and/or electron transfer between the

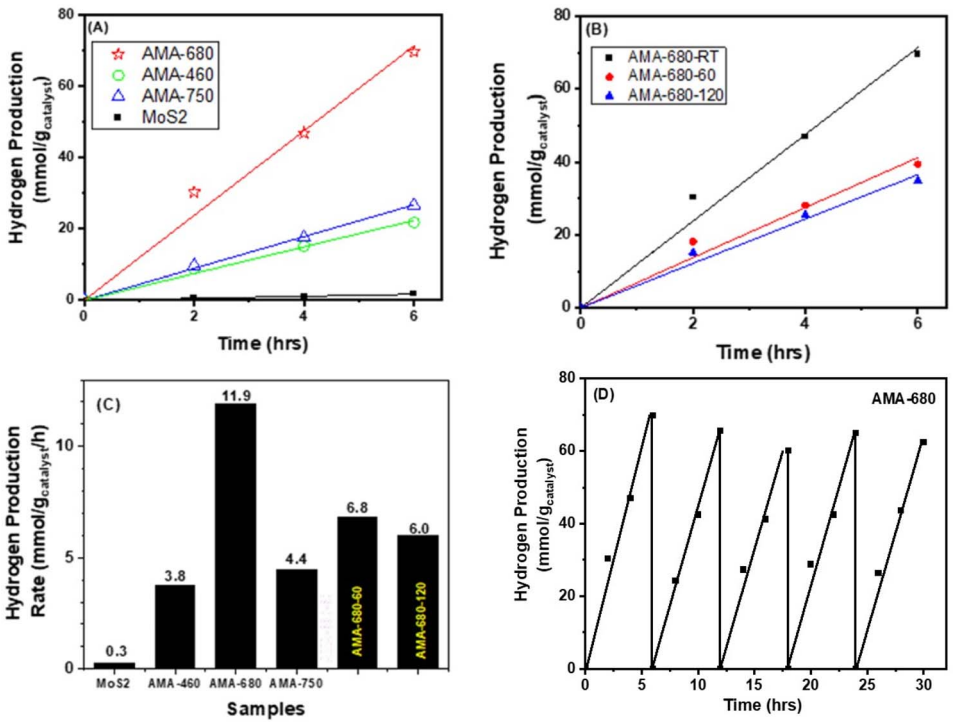

Fig. 5 Photocatalytic hydrogen evolution as a function of time over (A) AMA samples with Au nanocages with varying LSPR wavelengths and (B) AMA-680 samples treated at various temperatures. (C) Comparison of the photocatalytic hydrogen production rate over different samples. (D) Cycle stability test result of AMA-680 in photocatalytic hydrogen evolution.

Au-680 nanocages and the MoS_2 nanosheets. A more detailed discussion will be presented in the following part of this paper regarding the mechanism. Fig. 5D shows the cycling stability of AMA-680 in the photocatalytic HER, where above 90% of the activity can be preserved after 5 cycles. This indicates that the Au–MoS_2 composite is highly stable under the testing conditions.

To reveal the role played by the multiphases feature of MoS_2 in this reaction, AMA-680 is heated to 60 and 120 °C to vary the ratio of the 1T-like and 2H phases and tested for HER performance. As shown in Fig. 5B, the heat treatment, which leads to a decreased proportion of the 1T-like phase as shown in Table S1,‡ results in a decrease in the HER rate from 11.9 to 6.8 and 6.0 mmol H_2 $g_{catalyst}^{-1}$ h^{-1} for AMA-680, -60, and -120, respectively (Fig. 5C). The observation suggests an important role of the 1T-like phase in the HER, consistent with our previous result.[8] We previously showed that the photogenerated electrons from the 2H phase of MoS_2 had the tendency to diffuse to the 1T-like phase, where the protons were more likely to be reduced into hydrogen. The 1T-like metallic phase of MoS_2 is known as a good "electron sink" and exhibits superior electron affinity to the 2H phase MoS_2. Hence, the electrons generated, no matter the origin, are inclined to migrate to the 1T-like MoS_2 to conduct the HER. But the HER rate of AMA-680-60 and AMA-680-120 is still ~50% higher than that of the AMA-460 and AMA-750 samples, again pointing to the key role of the match between Au nanocage LSPR wavelength and the MoS_2 absorption edge.

Mechanism discussion

In order to unveil the origin of the excited electrons, time-resolved transient absorption spectroscopy (TAS) is carried out to track the destiny of the electrons in the AMA system. In this work, a 400 nm, 45 fs laser pulse is used as the pump to excite the electrons in AMA samples and the time-resolved differential transmission spectra were recorded to track the decay dynamics of the excited electrons. The transient absorption spectra recorded 0.4 ps after excitation are shown in Fig. 6A. They contain a broad feature with a positive sign (pointing up). Within this band, there are two depletion signals (pointing down) at around 660 and 610 nm originating from excitons A and B of MoS_2, respectively.[51,52] The broad positive band contains two peaks at around 500 (strong) and 700 nm (weak). Considering that the UV-vis spectra of the three samples also showed strong absorption around these two wavelengths, we monitored the three samples at 495 and 730 nm up to a 1 ns time-delay after the probe excitation and plotted their decay dynamics as functions of time in Fig. 6B and C in order to get better signals as well as facilely inspect the electron transfer mechanism under the excitation on and off the LSPR wavelength of Au nanocages. According to previous reports,[53,54] excitons in 2D-TMDs decay through three distinct mechanisms: a fast process ascribed to thermalization taking place within the first few picoseconds after excitation, followed by relaxation during the next few picoseconds, and finally a much slower process that can take hundreds of picoseconds or longer assigned to defect-assisted recombination. Based on this, we fitted the dynamics shown in Fig. 6B and C to the following tri-exponential decay function:

$$A_1 e^{-\frac{t}{t_1}} + A_2 e^{-\frac{t}{t_2}} + A_3 e^{-\frac{t}{t_3}}$$

t_1, t_2, and t_3 (ps) are the time-constants assigned to thermalization, relaxation and defect-assisted recombination processes, respectively, and A_1, A_2 and A_3 (milli optical density, mOD) are their corresponding amplitudes. All three time constants can be affected if there is any electron/energy transfer taking place at the MoS_2/Au nanocage interface. However, in this material system, only t_1 is the direct indicator of the LSPR effect since the plasmonic energy and/or hot electrons are mostly available during the first few hundreds of femtoseconds after the excitation, which is within the scope of t_1. As t_2 and t_3 represent slower processes, they are good indicators of the classic electron transfer from MoS_2 to Au nanocages as this process is not efficient enough to affect t_1. The fitted time constants are listed in Table 1 while the corresponding amplitudes are listed in Table S2.‡

A detailed discussion of the fitting results is given in the ESI.‡ Briefly, based on the fitted time constants, the AMA-460 system is a classic heterojunction photocatalyst system with Au-460 being the metal cocatalyst (as shown in Fig. S6A‡).

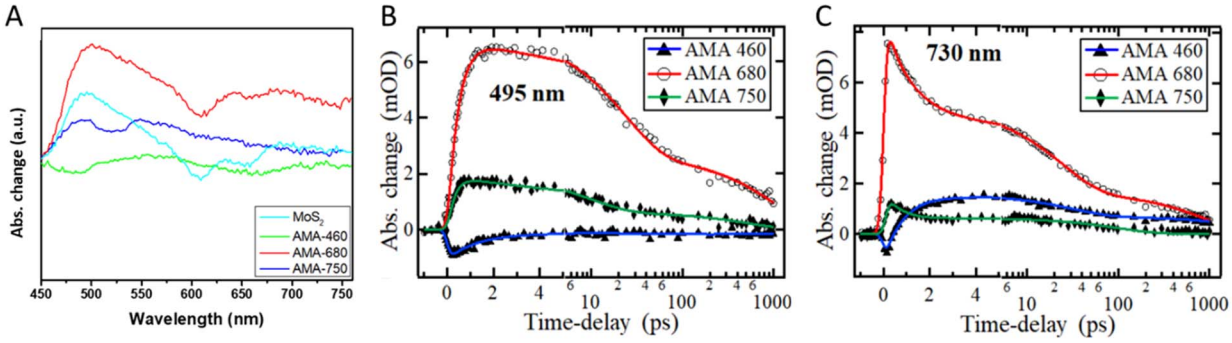

Fig. 6 (A) Transient absorption spectra of the AMA samples and bare MoS_2 (recorded at 0.4 ps after excitation at 400 nm) and transient absorption dynamics for AMA samples monitored at (B) 495 nm and (C) 730 nm following pump excitation at 400 nm. Symbols show experimental data, and solid plots show fits. The time-delay axis is shown on a linear scale up to 5 ps and logarithmic scale thereafter.

Table 1 Fitted results of three times constants (ps) of the AMA samples monitored at 495 and 730 nm

Time constant (ps)	Au-680	MoS_2	AMA-460	AMA-680	AMA-750
t_1-495	2.21	0.43	0.88	0.48	0.33
t_1-730	5.36	0.17	0.89	1.40	0.18
t_2-495	3.48	18.58	30.53	22.85	9.70
t_2-730	5.37	8.17	30.23	26.40	0.51
t_3-495	7044	1011	2940	1010	516
t_3-730	2267	788	2915	960	99

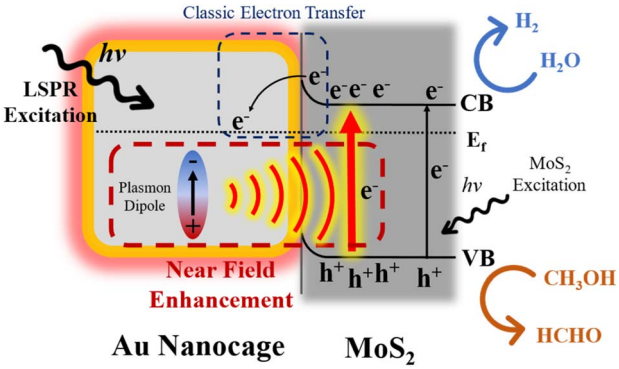

Fig. 7 Scheme of the proposed working mechanisms of AMA-680. CB: conduction band; VB: valence band.

However, as Au is usually not considered a great cocatalyst for the HER,[55] it cannot enhance the activity significantly. Meanwhile, the LSPR effect in AMA-750 just becomes strong enough to marginally overcome the classic electron transfer process (as shown in Fig. S6C‡). Although it converts the system to a plasmonic photocatalyst system, it does not show much enhancement in activity as well due to the overall weak LSPR effect. Unlike AMA-750, AMA-680 is thought to be a LSPR-dominant system (as shown in Fig. S6B‡). Unlike other samples, the decay behavior (depicted using the three time constants in Table 1) of AMA-680 is more analogous to that of Au nanocages, not MoS_2, which suggests that it is strongly affected by LSPR. It also exhibits much longer t_1 (t_1-730, 1.4 ns) around its LSPR wavelength than AMA-750 (t_1-730, 0.18 ns) and AMA-460 (t_1-730, 0.89 ns). As t_1 is the indicator of the LSPR effect, it further confirms that AMA-680 has a stronger LSPR effect than AMA-750 and AMA-460, which can account for its highest photocatalytic activity.

As stated in the introduction, there are potentially several LSPR processes working simultaneously in the plasmonic photocatalyst system, namely HET, NFE and PRET. If we assume that the classic electron transfer efficiency is identical for all three AMA systems (as they are prepared in the same way, the contact between Au and MoS_2 should be similar), the LSPR effect in the three systems follows the order AMA-680 > AMA-750 > AMA-460 (expressed in Fig. S6‡ by the weight of arrows) according to the transient absorption results. Importantly, it should be noticed that the approximations of their LSPR wavelength to the absorption edge of MoS_2 follow exactly the same order. Based on the introduction part, NFE is the only process whose efficiency relies on the match of LSPR wavelength with the absorption edge of the semiconductor. Therefore, the results strongly show that NFE is the dominant LSPR process in this system. Meanwhile, the HET process was significantly suppressed probably due to the insufficient direct contact between Au nanocages and MoS_2 stated above. For the PRET process, although it does not require a direct contact, the bare MoS_2 nanosheets around Au nanocages impose a strong FRET effect, nullifying the PRET effect. NFE, however, has no competing process and can affect an area that is 50 nm away[22] hence dominating the LSPR process in the AMA-680 system.

Based on the above discussion, a possible mechanism is illustrated for the LSPR promoted photocatalytic hydrogen evolution reaction in the Au/MoS_2 composite as shown in Fig. 7. For simplicity, only AMA-680 is presented and the 1T-like MoS_2 phase is not shown. Under the illumination of visible light, Au-680 and MoS_2 nanosheets will be excited simultaneously. Some electrons located at the conduction band (CB) of MoS_2 will migrate to the Fermi level (E_f) of Au-680 by overcoming the Schottky barrier at the interface. Meanwhile, the surface plasma on Au-680 will promote the generation of electron–hole pairs in MoS_2 through the NFE process. As the LSPR wavelength of Au-680 significantly matches the absorption edge of MoS_2 nanosheets, the ultraefficient NFE process completely dominates AMA-680 and hence, significantly enhances the photocatalytic performance. In our previous study on single layer multiphasic MoS_2, we showed that the 1T-like phase of MoS_2 is more favorable for electron acceptation and hydrogen evolution. Hence, with the presence of 1T-like MoS_2, all the excited electrons in this catalyst system are more inclined and readily transfer to the 1T-like MoS_2 region. Through such a synergy between the LSPR effect and the favorable phase structure of MoS_2, photon energy can be efficiently utilized for the hydrogen evolution reaction.

Conclusions

We demonstrate that visible-light-driven photocatalytic hydrogen generation can be greatly enhanced by creating heterojunctions between plasmonic Au nanocages and multiphasic single-layer MoS_2 nanosheets. We investigate Au nanocages with various LSPR wavelengths in order to understand the effect of the LSPR wavelength in relation to the optical absorption of MoS_2 on the photocatalytic hydrogen evolution reaction. The introduction of Au nanocages generally enhances the hydrogen evolution rate of the 2D MoS_2 nanosheets. Interestingly, the sample loaded with Au nanocages with the LSPR wavelength at 680 nm displays an impressive 40-fold increase in the HER rate compared to the bare MoS_2 nanosheets. The results from time-resolved TAS suggest that the key to this enhancement is related to the ultraefficient energy transfer from Au nanocages to MoS_2 through the near field enhancement process when the LSPR wavelength of Au nanocages matches the light absorption edge of MoS_2. This finding demonstrates a potential general strategy for designing plasmonic photocatalysts that have high activity under visible light irradiation for solar-to-fuel conversion.

Author contributions

R. Peng: investigation, data curation, formal analysis, methodology, writing – original draft; X. Ma: investigation, data curation, formal analysis, writing – review & editing; Z. Hood: data curation, methodology, writing – review and editing; A. Boulesbaa and A. Puretzky: data curation, formal analysis, writing – review & editing; J. Tong: writing – review & editing; Z. Wu: conceptualization, funding acquisition, project administration, writing – review & editing.

Conflicts of interest

There are no conflicts to declare.

Acknowledgements

This research was supported by the Center for Nanophase Materials Sciences (CNMS), which is a US Department of Energy, Office of Science User Facility at Oak Ridge National laboratory. Z. D. H. was supported by Laboratory Directed Research and Development (LDRD) funding from Argonne National Laboratory, provided by the Director, Office of Science, of the U.S. Department of Energy under Contract No. DE-AC02-06CH11357.

Notes and references

1 S. Das, M. Kim, J. W. Lee and W. Choi, *Crit. Rev. Solid State Mater. Sci.*, 2014, **39**, 231–252.
2 M.-R. Gao, Y.-F. Xu, J. Jiang and S.-H. Yu, *Chem. Soc. Rev.*, 2013, **42**, 2986–3017.
3 C. N. R. Rao, H. S. S. Ramakrishna Matte and U. Maitra, *Angew. Chem., Int. Ed.*, 2013, **52**, 13162–13185.
4 M. Chhowalla, H. S. Shin, G. Eda, L.-J. Li, K. P. Loh and H. Zhang, *Nat. Chem.*, 2013, **5**, 263–275.
5 T. Su, Q. Shao, Z. Qin, Z. Guo and Z. Wu, *ACS Catal.*, 2018, **8**, 2253–2276.
6 P. Afanasiev, *C. R. Chim.*, 2008, **11**, 159–182.
7 E. Benavente, M. A. Santa Ana, F. Mendizábal and G. González, *Coord. Chem. Rev.*, 2002, **224**, 87–109.
8 R. Peng, L. Liang, Z. D. Hood, A. Boulesbaa, A. Puretzky, A. V. Ievlev, J. Come, O. S. Ovchinnikova, H. Wang, C. Ma, M. Chi, B. G. Sumpter and Z. Wu, *ACS Catal.*, 2016, **6**, 6723–6729.
9 G. Eda, H. Yamaguchi, D. Voiry, T. Fujita, M. Chen and M. Chhowalla, *Nano Lett.*, 2011, **11**, 5111–5116.
10 G. Eda, T. Fujita, H. Yamaguchi, D. Voiry, M. Chen and M. Chhowalla, *ACS Nano*, 2012, **6**, 7311–7317.
11 M. Kan, J. Y. Wang, X. W. Li, S. H. Zhang, Y. W. Li, Y. Kawazoe, Q. Sun and P. Jena, *J. Phys. Chem. C*, 2014, **118**, 1515–1522.
12 Y.-C. Lin, D. O. Dumcenco, Y.-S. Huang and K. Suenaga, *Nat. Nanotechnol.*, 2014, **9**, 391–396.
13 L. Cai, J. He, Q. Liu, T. Yao, L. Chen, W. Yan, F. Hu, Y. Jiang, Y. Zhao, T. Hu, Z. Sun and S. Wei, *J. Am. Chem. Soc.*, 2015, **137**, 2622–2627.
14 Y. Tian and T. Tatsuma, *J. Am. Chem. Soc.*, 2005, **127**, 7632–7637.
15 K. Awazu, M. Fujimaki, C. Rockstuhl, J. Tominaga, H. Murakami, Y. Ohki, N. Yoshida and T. Watanabe, *J. Am. Chem. Soc.*, 2008, **130**, 1676–1680.
16 J. L. Yang, Y. L. He, H. Ren, H. L. Zhong, J. S. Lin, W. M. Yang, M. D. Li, Z. L. Yang, H. Zhang, Z. Q. Tian and J. F. Li, *ACS Catal.*, 2021, **11**, 5047–5053.
17 H. Tada, *Nanoscale Adv.*, 2019, **1**, 4238–4245.
18 D. V. Dao, T. T. D. Nguyen, P. Uthirakumar, Y. H. Cho, G. C. Kim, J. K. Yang, D. T. Tran, T. D. Le, H. Choi, H. Y. Kim, Y. T. Yu and I. H. Lee, *Appl. Catal., B*, 2021, **286**, 119947.
19 A. Kumar, P. Choudhary, A. Kumar, P. H. C. Camargo and V. Krishnan, *Small*, 2022, **18**, e2101638.
20 X. C. Ma, Y. Dai, L. Yu and B. B. Huang, *Light: Sci. Appl.*, 2016, **5**, e16017.
21 Z. Ye, Z. Xu, W. Yue, X. Liu, L. Wang and J. Zhang, *Phys. Chem. Chem. Phys.*, 2023, 2706–2716, DOI: **10.1039/d2cp04582f**.
22 W. R. Erwin, H. F. Zarick, E. M. Talbert and R. Bardhan, *Energy Environ. Sci.*, 2016, **9**, 1577–1601.
23 J. T. Li, S. K. Cushing, F. K. Meng, T. R. Senty, A. D. Bristow and N. Q. Wu, *Nat. Photonics*, 2015, **9**, 601–607.
24 C. L. Wang and D. Astruc, *Chem. Soc. Rev.*, 2014, **43**, 7188–7216.
25 N. L. Reddy, V. N. Rao, M. Vijayakumar, R. Santhosh, S. Anandan, M. Karthik, M. V. Shankar, K. R. Reddy, N. P. Shetti, M. N. Nadagouda and T. M. Aminabhavi, *Int. J. Hydrogen Energy*, 2019, **44**, 10453–10472.
26 Y. Shi, J. Wang, C. Wang, T.-T. Zhai, W.-J. Bao, J.-J. Xu, X.-H. Xia and H.-Y. Chen, *J. Am. Chem. Soc.*, 2015, **137**, 7365–7370.
27 I. Irfan, S. Golovynskyi, O. A. Yeshchenko, M. Bosi, T. Zhou, B. Xue, B. K. Li, J. L. Qu and L. Seravalli, *Physica E*, 2022, **140**, 115213.
28 R. Bar-Ziv, P. Ranjan, A. Lavie, A. Jain, S. Garai, A. Bar Hen, R. Popoyitz-Biro, R. Tenne, R. Arenal, A. Ramasubramaniam, L. Lajaunie and M. Bar-Sadan, *ACS Appl. Energy Mater.*, 2019, **2**, 6043–6050.
29 M. Garai, Z. Y. Zhu, J. Shi, S. S. Li and Q. H. Xu, *J. Chem. Phys.*, 2021, **155**, 234201.
30 S. Najmaei, A. Mlayah, A. Arbouet, C. Girard, J. Léotin and J. Lou, *ACS Nano*, 2014, **8**, 12682–12689.
31 J. Li, Z. Chen, H. Yang, Z. Yi, X. Chen, W. Yao, T. Duan, P. Wu, G. Li and Y. Yi, *Nanomaterials*, 2020, **10**, 257.
32 S. H. Wang, Y. Zhang, Y. Y. Zheng, Y. B. Xu, G. D. Yang, S. X. Zhong, Y. L. Zhao and S. Bai, *Small*, 2023, **19**, 2204774.
33 Y. Yu, Z. Ji, S. Zu, B. Du, Y. Kang, Z. Li, Z. Zhou, K. Shi and Z. Fang, *Adv. Funct. Mater.*, 2016, **26**, 6394–6401.
34 X. Yang, W. Liu, M. Xiong, Y. Zhang, T. Liang, J. Yang, M. Xu, J. Ye and H. Chen, *J. Mater. Chem. A*, 2014, **2**, 14798–14806.
35 Y. Kang, S. Najmaei, Z. Liu, Y. Bao, Y. Wang, X. Zhu, N. J. Halas, P. Nordlander, P. M. Ajayan, J. Lou and Z. Fang, *Adv. Mater.*, 2014, **26**, 6467–6471.
36 A. Rani, A. S. Patel, A. Chakraborti, K. Singh and P. Sharma, *J. Mater. Sci.: Mater. Electron.*, 2021, **32**, 6168–6184.

37 E. Thimsen, F. Le Formal, M. Grätzel and S. C. Warren, *Nano Lett.*, 2011, **11**, 35–43.
38 G. Collins, A. Lonergan, D. McNulty, C. Glynn, D. Buckley, C. Y. Hu and C. O'Dwyer, *Adv. Mater. Interfaces*, 2020, **7**, 1901805.
39 J. T. Li, S. K. Cushing, J. Bright, F. K. Meng, T. R. Senty, P. Zheng, A. D. Bristow and N. Q. Wu, *ACS Catal.*, 2013, **3**, 47–51.
40 X. Yue, J. Hou, Y. Zhang, P. Wu, Y. Guo, S. Peng, Z. Liu and H. Jiang, *Dalton Trans.*, 2020, **49**, 7467–7473.
41 S. E. Skrabalak, L. Au, X. D. Li and Y. N. Xia, *Nat. Protoc.*, 2007, **2**, 2182–2190.
42 H. M. Zhang, T. Zhu and M. Li, *J. Phys. Chem. Lett.*, 2023, **14**, 3853–3860.
43 Q. Zhang, W. Li, L. P. Wen, J. Chen and Y. Xia, *Chem. –Eur. J.*, 2010, **16**, 10234–10239.
44 S. E. Skrabalak, L. Au, X. Li and Y. Xia, *Nat. Protoc.*, 2007, **2**, 2182.
45 S. E. Skrabalak, J. Chen, Y. Sun, X. Lu, L. Au, C. M. Cobley and Y. Xia, *Acc. Chem. Res.*, 2008, **41**, 1587–1595.
46 A. Boulesbaa, B. Huang, K. Wang, M.-W. Lin, M. Mahjouri-Samani, C. Rouleau, K. Xiao, M. Yoon, B. Sumpter, A. Puretzky and D. Geohegan, *Phys. Rev. B: Condens. Matter Mater. Phys.*, 2015, **92**, 115443.
47 C. Lee, H. Yan, L. E. Brus, T. F. Heinz, J. Hone and S. Ryu, *ACS Nano*, 2010, **4**, 2695–2700.
48 U. Gupta, B. S. Naidu, U. Maitra, A. Singh, S. N. Shirodkar, U. V. Waghmare and C. N. R. Rao, *APL Mater.*, 2014, **2**, 092802.
49 S. Mubeen, J. Lee, N. Singh, S. Krämer, G. D. Stucky and M. Moskovits, *Nat. Nanotechnol.*, 2013, **8**, 247.
50 S. Linic, P. Christopher and D. B. Ingram, *Nat. Mater.*, 2011, **10**, 911.
51 Y. Yu, Y. Yu, Y. Cai, W. Li, A. Gurarslan, H. Peelaers, D. E. Aspnes, C. G. Van de Walle, N. V. Nguyen, Y.-W. Zhang and L. Cao, *Sci. Rep.*, 2015, **5**, 16996.
52 S. Sim, J. Park, J.-G. Song, C. In, Y.-S. Lee, H. Kim and H. Choi, *Phys. Rev. B: Condens. Matter Mater. Phys.*, 2013, **88**, 075434.
53 Z. E. Eroglu, D. Contreras, P. Bahrami, N. Azam, M. Mahjouri-Samani and A. Boulesbaa, *Nanomaterials*, 2021, **11**, 770.
54 Z. E. Eroglu, O. Comegys, L. S. Quintanar, N. Azam, S. Elafandi, M. Mahjouri-Samani and A. Boulesbaa, *Phys. Chem. Chem. Phys.*, 2020, **22**, 17385–17393.
55 C. J. Li, O. J. H. Chai, Q. F. Yao, Z. H. Liu, L. Wang, H. J. Wang and J. P. Xie, *Mater. Horiz.*, 2021, **8**, 1657–1682.